

Antideuteron and deuteron production in mid-central Pb+Pb collisions at 158A GeV

T. Anticic,²² B. Baatar,⁸ D. Barna,⁴ J. Bartke,⁶ H. Beck,⁹ L. Betev,¹⁰ H. Białkowska,¹⁹ C. Blume,⁹ M. Bogusz,²¹ B. Boimska,¹⁹ J. Book,⁹ M. Botje,¹ P. Bunčić,¹⁰ T. Cetner,²¹ P. Christakoglou,¹ P. Chung,¹⁸ O. Chvala,¹⁴ J.G. Cramer,¹⁵ V. Eckardt,¹³ Z. Fodor,⁴ P. Foka,⁷ V. Friese,⁷ M. Gaździcki,^{9,11} K. Grebieszko,²¹ C. Höhne,⁷ K. Kadija,²² A. Karev,¹⁰ V.I. Kolesnikov,⁸ M. Kowalski,⁶ D. Kresan,⁷ A. Laszlo,⁴ R. Lacey,¹⁸ M. van Leeuwen,¹ M. Maćkowiak-Pawłowska,²¹ M. Makariev,¹⁷ A.I. Malakhov,⁸ M. Mateev,¹⁶ G.L. Melkumov,⁸ M. Mitrovski,⁹ St. Mrówczyński,¹¹ V. Nikolic,²² G. Pála,⁴ A.D. Panagiotou,² W. Peryt,²¹ J. Pluta,²¹ D. Prindle,¹⁵ F. Pühlhofer,¹² R. Renfordt,⁹ C. Roland,⁵ G. Roland,⁵ M. Rybczyński,¹¹ A. Rybicki,⁶ A. Sandoval,⁷ N. Schmitz,¹³ T. Schuster,⁹ P. Seyboth,¹³ F. Siklér,⁴ E. Skrzypczak,²⁰ M. Slodkowski,²¹ G. Stefanek,¹¹ R. Stock,⁹ H. Ströbele,⁹ T. Susa,²² M. Szuba,²¹ M. Utvić,⁹ D. Varga,³ M. Vassiliou,² G.I. Veres,⁴ G. Vesztergombi,⁴ D. Vranić,⁷ Z. Włodarczyk,¹¹ and A. Wojtaszek-Szwarc¹¹

(The NA49 Collaboration)

¹*NIKHEF, Amsterdam, Netherlands.*

²*Department of Physics, University of Athens, Athens, Greece.*

³*Eötvös Loránt University, Budapest, Hungary.*

⁴*KFKI Research Institute for Particle and Nuclear Physics, Budapest, Hungary.*

⁵*MIT, Cambridge, USA.*

⁶*H. Niewodniczański Institute of Nuclear Physics,
Polish Academy of Sciences, Cracow, Poland.*

⁷*Gesellschaft für Schwerionenforschung (GSI), Darmstadt, Germany.*

⁸*Joint Institute for Nuclear Research, Dubna, Russia.*

⁹*Fachbereich Physik der Universität, Frankfurt, Germany.*

¹⁰*CERN, Geneva, Switzerland.*

¹¹*Institute of Physics, Jan Kochanowski University, Kielce, Poland.*

¹²*Fachbereich Physik der Universität, Marburg, Germany.*

¹³*Max-Planck-Institut für Physik, Munich, Germany.*

¹⁴*Inst. of Particle and Nuclear Physics,*

Charles Univ., Prague, Czech Republic.

¹⁵*Nuclear Physics Laboratory, University of Washington, Seattle, WA, USA.*

¹⁶*Atomic Physics Department, Sofia University St. Kliment Ohridski, Sofia, Bulgaria.*

¹⁷*Institute for Nuclear Research and Nuclear Energy, BAS, Sofia, Bulgaria.*

¹⁸*Department of Chemistry, Stony Brook Univ. (SUNYSB), Stony Brook, USA.*

¹⁹*National Center for Nuclear Research, Warsaw, Poland.*

²⁰*Institute for Experimental Physics,*

University of Warsaw, Warsaw, Poland.

²¹*Faculty of Physics, Warsaw University of Technology, Warsaw, Poland.*

²²*Rudjer Boskovic Institute, Zagreb, Croatia.*

(Dated: January 10, 2021)

(DRAFT 2.0)

Abstract

Production of deuterons and antideuterons was studied by the NA49 experiment in the 23.5% most central Pb+Pb collisions at the top SPS energy of $\sqrt{s_{\text{NN}}}=17.3$ GeV. Invariant yields for \bar{d} and d were measured as a function of centrality in the center-of-mass rapidity range $-1.2 < y < -0.6$. Results for $\bar{d}(d)$ together with previously published $\bar{p}(p)$ measurements are discussed in the context of the coalescence model. The coalescence parameters B_2 were deduced as a function of transverse momentum p_t and collision centrality.

PACS numbers: 25.75.Dw

I. INTRODUCTION

Studies of antideuteron and deuteron production in heavy-ion collisions are attractive for many reasons. Enhanced antimatter production in central nucleus-nucleus collisions relative to $p + p$ was proposed as one of the experimental signatures for formation of a new state of strongly interacting nuclear matter - the Quark-Gluon Plasma. [1–3]. If antibaryon abundances are not in equilibrium or not strongly affected by annihilation after chemical freeze-out, some of the initial enhancement may survive till the final stage of the collision process. However, at SPS energies baryon rich nuclear matter is created at high temperatures ($\mu_B \approx 250$ MeV and $T \approx 160$ MeV in central Pb+Pb collisions at 158A GeV [4]). In a hadronic medium of such temperature and baryon density, reaction rates involving antibaryons will be high due to annihilation and multi-pion fusion processes [5–7]. Thus any antimatter enhancement from the partonic phase or its transition to the hadronic phase is likely to survive only if freeze-out occurs right after the phase transition.

At the late stage of the fireball evolution, when the hadronic matter is diluted enough such that secondary inelastic collisions cease, the observed clusters are formed from nucleons. The process of nucleosynthesis in strongly interacting systems heated to more than 100 MeV was extensively studied over the past years for species ranging from $A=2$ to $A=7$ [8–13]. Recently, the formation of (anti)hypernuclei was observed in Au+Au collisions by the E864 experiment at AGS energies [14] and by the STAR collaboration at RHIC [15].

In a simplified coalescence approach [16, 17], (anti)nucleon bound states are formed from (anti)nucleons which are close in momentum and configuration space. Their production is usually characterized by the coalescence factor B_A which relates the invariant yield of a cluster of size A to the A^{th} power of the proton yield. The B_2 parameter for deuterons was found to be approximately constant in heavy-ion collisions at beam energies below 1A GeV as well as in all proton-induced reactions. However, at higher collision energies (more than several GeV per nucleon) the diameter of the source created in central collisions is much larger than the deuteron size due to expansion of the reaction zone, and the cluster production process becomes sensitive to the details of the phase-space distribution of the constituents. In particular, a strong collective radial flow (the average transverse velocity is about $0.5c$ at SPS energies [18]) produces correlations between the production point in space-time and the momentum of the clusters. Thus, an interplay between the flow velocity

profile and the nucleon density distribution may result in different shapes of transverse momentum spectra for composites and single nucleons [19]. A comparative analysis of the production of clusters made of nucleons and antinucleons might therefore provide insight into the details of the fireball evolution and the nucleon phase-space distribution at kinetic freeze-out. The production rate of composites should depend on the spatial distribution of their constituents. If the \bar{p} suffer from annihilation in the dense baryonic matter, this could therefore be reflected in the impact parameter dependence of the \bar{d} yield [20]. Moreover, because of the additional annihilation cross section, \bar{d} are expected to decouple from their source at much lower hadron density than d and therefore their freeze-out volume is expected to be larger. In summary, the study of \bar{d} and d production provides an alternate method for extracting information about the source size [21, 22] which is complementary to the femtoscopy approach.

Recently, NA49 reported [23] on \bar{p} production at midrapidity in centrality selected Pb+Pb collisions at 158A GeV. In the following we extended this study of antimatter to the investigation of heavier systems. This paper reports our measurement of \bar{d} and d invariant yields around midrapidity in the same reaction.

The paper is organized as follows. The next section gives an overview of the NA49 experimental set-up. Details of the data analysis procedure are described in Section III. In Section IV we present and discuss the results on \bar{d} and d production in mid-central Pb+Pb collisions. A summary is given in the last section.

II. EXPERIMENTAL SETUP

The NA49 apparatus was designed as a large acceptance magnetic spectrometer to study nucleus-nucleus collisions in the SPS energy range. The NA49 setup covers about 50% of the final state phase space for Pb+Pb reactions at a beam energy of 158A GeV. The detector provides precise tracking and robust particle identification. A full description of the apparatus components can be found in Ref. [24].

The primary lead beam was extracted from the CERN Super Proton Synchrotron (SPS) and delivered to NA49 through the H2 beam line in the SPS North Area. The intensity of the beam (delivered in spills 4.8 s long) was typically $10^5/s$. The beam was defined within the experiment by a set of Cherenkov and scintillation counters placed along 35 m of the

beam path upstream from the nominal target position. The transverse diameter of the beam spot on the target, as measured by three multi-wire proportional beam position detectors (BPDs), was about 1 mm. The target was a lead foil of 337 mg/cm² thickness (1.5% of a Pb interaction length). The interaction trigger required a valid beam signal plus a collision centrality tag based on the measurement of projectile spectator energy registered in the zero-degree calorimeter VCAL which was placed 23 m downstream of the target.

Charged reaction products originating from the interaction vertex are recorded by four gas Time Projection Chambers (TPCs). Two Vertex TPCs (VTPC), serving mainly for momentum analysis, are located inside two superconducting dipole magnets, which provide a magnetic field with a total bending power of about 9 Tm. The two Main TPCs (MTPC), with about 27 m³ gas volume each, are positioned behind the magnets on each side of the beam line. These TPCs are optimized for energy loss (dE/dx) measurements with a precision of 4% for minimum ionizing particles (*mip*).

Two Time-of-Flight (TOF) arrays (walls), positioned behind the MTPCs at ≈ 14 m from the interaction vertex, are the main detector systems used in this analysis for the identification of charged hadrons of momenta up to 10 GeV/ c . The TOF setup provides rapidity coverage of about 0.8 units in the mid-rapidity region and transverse momentum coverage up to $p_t = 2.5$ GeV/ c . Each wall consists of 891 pixels made of 2.5 cm thick plastic scintillators with transverse dimensions of 6, 7 and 8 cm (horizontal) by 3.4 cm (vertical). Each pixel is viewed by one phototube of 1.4 inch diameter glued to the side of the pixel. The phototube outputs (typically 1.5 Volts high for a charge = 1 *mip* passing through the pixel) are divided into two equal parts and digitized by TDCs and ADCs for time-of-flight and energy loss measurements, respectively. The least count of the FASTBUS LeCroy TDCs was set to 25 ps. Pixels are assembled in groups of 11 (as stacks in the vertical direction) in light-protected cassettes.

A 0.5 mm thick quartz Cherenkov counter S_1 placed 34 m upstream of the target provided the common start signals and the gates to the TDCs and ADCs, respectively. For a beam of lead nuclei S_1 has an intrinsic time resolution about 30 ps. The overall time resolution achieved with the TOF system was $\sigma \approx 60$ ps and allows for a 5σ p/d separation up to a momentum of $p = 10$ GeV/ c .

III. DATA ANALYSIS

A. Data sets

A high statistics sample of Pb+Pb collisions at beam energy of 158A GeV was collected during the year 2000 run period. A total of $2.4 \cdot 10^6$ events were recorded with an online event trigger selecting the 23.5% most central collisions.

TABLE I: Summary of the data sets used in the analysis. The number of events employed are given together with the fraction of the total cross-section (in percent) and corresponding average number of wounded nucleons $\langle N_w \rangle$ per event derived from the VENUS model.

centrality	$\langle N_w \rangle$	N_{events}
0-23.5%	265	2,400,000
0-12.5%	315	1,240,000
12.5-23.5%	211	1,160,000

To study the centrality dependence of the \bar{d} and d yields the data set was divided into two centrality classes (see Table I for detail). For each centrality selection, the corresponding number of wounded nucleons N_w as well as the percentage of the total cross-section were obtained from the Glauber model approach using a simulation with the VENUS event generator [25, 26].

B. Time of flight reconstruction

The analysis procedure starts with the calibration of all TOF pixels: time-zero offsets T_0 , ADC gains, and pedestals were determined. All reconstructed tracks in the TPCs with assigned momentum were extrapolated towards the TOF detectors and all possible associations between the track extrapolations and the calibrated TOF hits were found. For each TOF hit the raw TDC count was then corrected for the light propagation time in the scintillator according to the position of the point from which the light originated, and for the amplitude-dependent time-walk effect in the discriminator. The correction was as large as 50 ps/cm and 30 ps for the light propagation time and time-walk effect, respectively. Finally, an event-by-event global time offset (≈ 40 -50 ps on average) was determined as the

mean of the distribution of the differences between the measured and calculated arrival time for pions selected by their energy loss dE/dx in the TPCs (15 to 30 π 's per wall in an event depending on the collision centrality). The achieved overall time resolution of the TOF system was about 60 ps.

The squared mass m^2 was calculated from the reconstructed momentum p , the flight path to the TOF detector l and the measured time-of-flight t as

$$m^2 = \frac{p^2}{c^2} \left(\frac{c^2 t^2}{l^2} - 1 \right) \quad (1)$$

where c denotes the speed of light.

C. Event and track selection

In the following we discuss the event selection criteria as well as the track and TOF hit quality cuts which were applied during the analysis. In order to eliminate the background from non-target interactions an offline cut on the vertex z coordinate along the beam line was imposed. The difference between the z -position reconstructed from tracks and the nominal (survey) target position was required to be less than 1 cm ($\pm 4\sigma$ deviation, with σ being the RMS of the vertex z distribution). The fraction of events rejected by this cut was about 0.5%.

Track candidates were required to have a valid momentum fit result and dE/dx measurement. In order to reduce the contamination by background tracks from secondary interactions in the material or decays inside the TPC, the following track quality criteria were applied:

1. Tracks were accepted if they had points in the MTPC and in at least one of the VTPCs, and the length of the MTPC track segment was longer than 1.5 m.
2. Both vertical and horizontal deviations from the vertex position, after back extrapolation to the z position of the target, were required to be less than 1 cm.

An additional set of quality cuts was imposed to reject those TOF hits that have poorly reconstructed time of flight:

1. Candidates were rejected if two or more tracks in the event hit the same scintillator.

2. A distance greater than 1 mm from the pixel's edges was required for the position of a TOF hit to account for mismatches between TPC tracks and TOF signals due to multiple scattering and TPC-TOF misalignment.
3. A cut on the energy deposited in a scintillator was applied to reduce background under the (anti)deuteron mass peak due to false TOF hits and interactions of γ s associated to the interactions. The ADC value normalized to minimum ionizing particles was required to be within $0.8 < ADC/ADC_{mip} < 1.4$.

The fraction of the TOF hits remaining after all the quality cuts was found to be 67%.

D. Identification of deuterons and antideuterons

Particle identification is done in two steps by combining measurements of time-of-flight from the TOF detector and dE/dx from the MTPCs. First, the allowed values of dE/dx were limited to

$$dE/dx < dE/dx_{BB}(p) + k\sigma(p),$$

where $dE/dx_{BB}(p)$ is the most probable value as taken from a momentum dependent parameterization of the Bethe-Bloch curve for deuterons, and $\sigma(p)$ is the corresponding resolution in dE/dx . The parameter k was set to 3 and 2 for d and \bar{d} , respectively. As illustrated in Fig. 1 (left panel) for the momentum bin $7 < p < 8$ GeV/ c such a cut reduces the contribution of pions and kaons to the \bar{d} (d). The resulting m^2 -distributions for positively and negatively charged particles after applying the previously described quality and dE/dx PID cuts show clear d and \bar{d} peaks (Fig. 1, right panel). The entire track sample of $\bar{d}(d)$ was divided into transverse momentum bins of 0.15 GeV/ c width; the three highest p_t bins were combined into a wider one because of lack of statistics. In each p_t bin candidates are selected by a $\pm 3\sigma$ window in m^2 around the nominal position. The raw yields were determined by summing the histogram bin contents within the mass window. The background contamination under the \bar{d} (d) peak was evaluated by fitting the m^2 -distribution to a sum of a Gaussian signal and an exponential background. Figure 2 shows mass squared distributions along with the combined (Gauss + exponential) fits for \bar{d} for three p_t bins. The background contamination is weakly dependent on p_t and amounts to less than 3% for deuterons, but reaches $\approx 45\%$ for \bar{d} . The statistical error of the raw \bar{d} yields was calculated

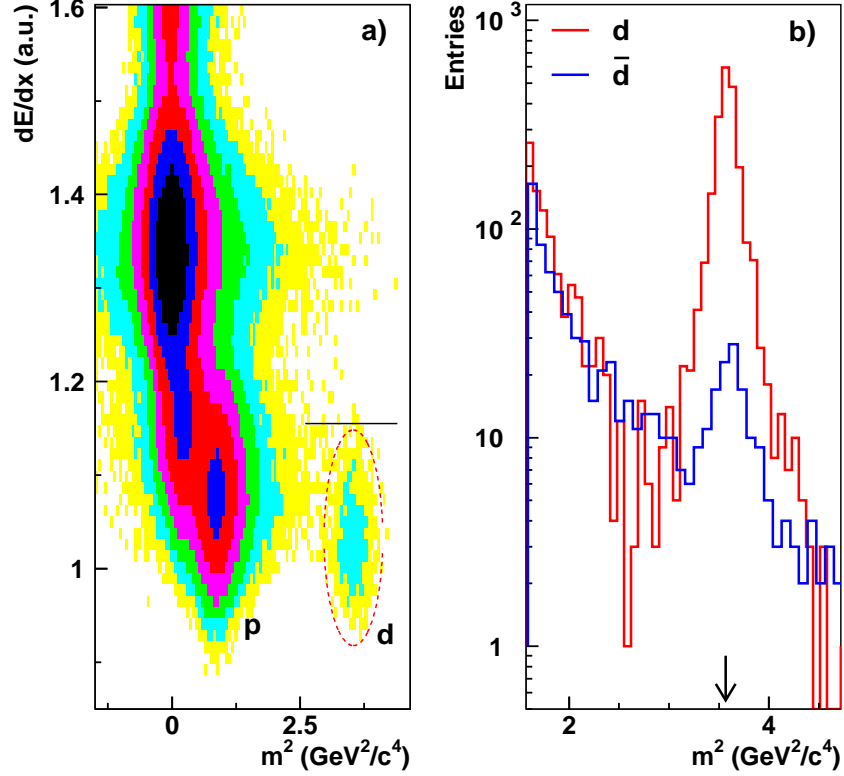


FIG. 1: (Color online) a) dE/dx versus m^2 for positively charged particles in the momentum interval $7 < p < 8$ GeV/ c . The dashed ellipse illustrates the region populated by deuterons; the PID upper-limit dE/dx cut is indicated by the horizontal line. b) m^2 -distributions for both charges around the m_d^2 position for momenta from 4 to 10 GeV/ c (dE/dx PID cut for $d(\bar{d})$ was applied). The arrow indicates the nominal m^2 position for $d(\bar{d})$.

as $\sqrt{N} = \sqrt{N_{\bar{d}} + N_{bkg}}$, where $N_{\bar{d}}$ and N_{bkg} are the number of \bar{d} and background counts, respectively.

E. Corrections

The raw yields were weighted by correction factors which account for the geometrical acceptance and for the losses due to the applied track quality and dE/dx PID cut.

Correction factors for the limited geometrical coverage of the detector system were obtained from a GEANT-based Monte Carlo simulation. Figure 3 shows the NA49 TOF

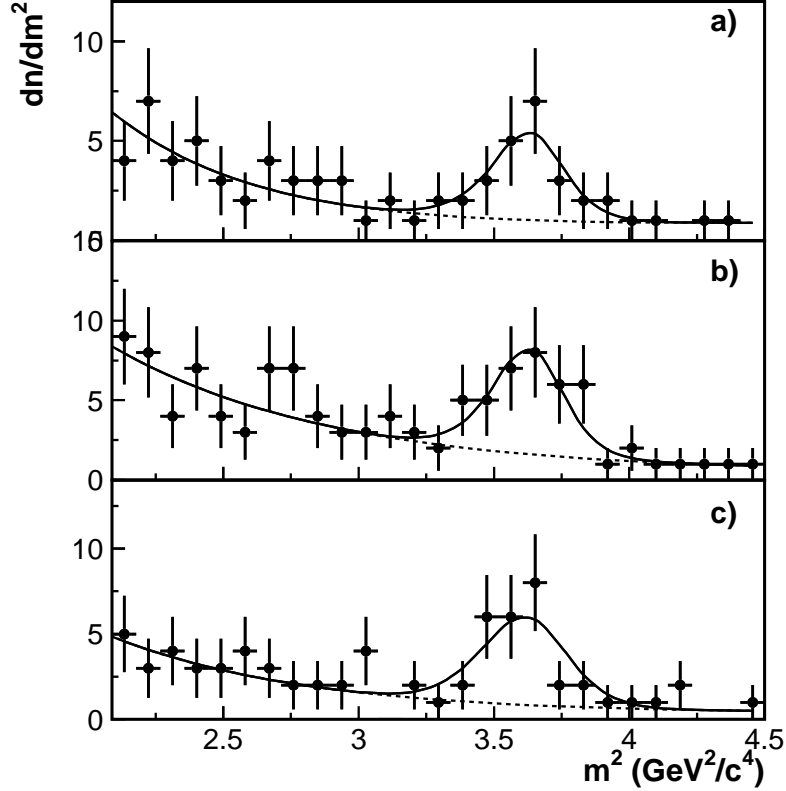


FIG. 2: Mass-squared distributions of \bar{d} for rapidity $-1.2 < y < -0.6$ in several transverse momentum bins: a) $0 < p_t < 0.3$ GeV/c, b) $0.3 < p_t < 0.45$ GeV/c, c) $0.45 < p_t < 0.6$ GeV/c. Solid lines represent fits of a sum of a Gaussian signal and an exponential background.

acceptance for $d(\bar{d})$ in terms of transverse momentum p_t and center-of-mass rapidity y . The bin size was taken to be $\Delta y=0.1$ by $\Delta p_t=25$ MeV/c, and all the bins at the edges of the acceptance were rejected to avoid a very large correction factor. The acceptance drops down to about 6% at $p_t > 0.6$ GeV/c. Monte Carlo studies with simulated tracks embedded into real data showed that the tracking reconstruction efficiency in the phase-space region covered by the TOF detector is above 98%. All remaining corrections were determined from the data in bins of p_t . For each centrality bin the corrections for multihits were obtained by determining the fraction of tracks rejected by the requirement that only a single one hits a scintillator. This correction shows less than 3% variation with centrality and is on average 11% and 8% for the 0-12.5% and 12.5-23.5% most central events, respectively. The losses due to the geometrical fiducial cut (1 mm edge cut) were determined averaged over all cen-

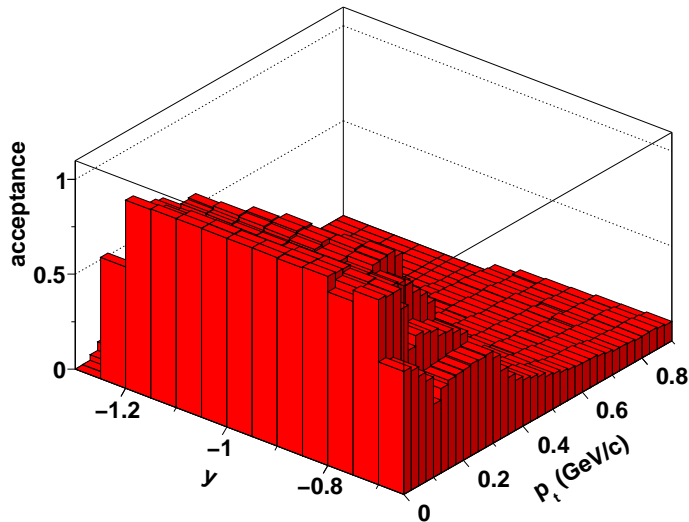


FIG. 3: (Color online) Geometrical TOF acceptance as a function of rapidity y and transverse momentum p_t for d at 158A GeV.

tralities. This correction accounts for about 9% losses. The corrections (about 15%) due to the pulse height constraint ($0.8 < ADC/ADC_{mip} < 1.4$) were determined for the deuteron sample and applied for both \bar{d} and d . The corrections for the losses due to the DCA cut ($\approx 2\%$) were also determined from the DCA distributions of the deuteron candidates.

F. Systematic errors

The systematic errors of the d and \bar{d} yields originate mainly from the uncertainties of particle identification and efficiency correction factors. In general, each particular contribution to the overall systematic error was estimated by varying the characteristic selection criteria, i.e., by loosening some cut or making it tighter. The contributions of the following selection criteria were studied: the dE/dx identification cut, the pulse height and geometrical cuts for selecting TOF hits and the DCA cut for selecting tracks. The uncertainty arising from the PID procedure for \bar{d} (including background subtraction) introduces a systematic error of the order of 13%. The DCA cut contributed $\approx 5\%$ to the overall systematic error. The error associated with the TOF efficiency correction for \bar{d} was found to be 9%.

The overall systematic error, obtained as the quadratic sum of all contributions, was

estimated to be 17% for \bar{d} and 10% for d .

IV. RESULTS AND DISCUSSION

A. Transverse momentum distributions

Figure 4 (a,b) shows the invariant yields of d and \bar{d} for centrality selected Pb+Pb collisions as a function of transverse momentum p_t . The yields are averaged over the center-of-mass rapidity interval $-1.2 < y < -0.6$. The data for the most central bin are shown to scale, while each successive distribution was divided by an additional factor of ten for clarity of presentation. We have also analyzed p and \bar{p} yields in the same centrality selected event samples. A detailed description of the analysis procedure for (anti)protons can be found elsewhere [23]. The invariant distributions for p and \bar{p} measured in the rapidity interval $-0.5 < y < -0.1$ are shown in Fig.4 (c,d). The yields agree with the previously published data [23] within 12%, the observed difference is mainly due to feed-down corrections from weak decays which are now based on the recent experimental data on $\Lambda(\bar{\Lambda})$ production from the NA49 experiment [27, 28]. Numerical values of the transverse momentum spectra are given in Table II.

Calculations using the microscopic transport model UrQMD [29] suggest that, due to annihilation in dense baryon matter, a considerable difference between the p_t distributions of anticlusters compared to those of clusters is expected. If annihilation of antimatter in the fireball medium affects \bar{d} production, then one would expect \bar{d} losses to be larger at midrapidity and at low p_t [30], resulting in a hardening of the p_t spectra of \bar{d} compared to those for d . On the other hand, the NA49 measurements of mid-rapidity $\bar{p}(p)$ spectra [23] show little difference between transverse distributions of p and \bar{p} for all centralities, leading to the conclusion that the p_t dependence (if any) of annihilation losses for antiprotons is small at 158A GeV. A similar behavior is also observed for the lambdas and antilambdas [28].

The experimental deuteron distributions were fitted to an exponential function in m_t (shown by curves in Fig. 4 (a))

$$\frac{1}{p_t} \frac{d^2N}{dp_t dy} = \frac{dN/dy}{T(m+T)} \exp\left(-\frac{m_t - m}{T}\right) \quad (2)$$

where dN/dy and T are two fit parameters, $m_t = \sqrt{p_t^2 + m^2}$ is the transverse mass and m

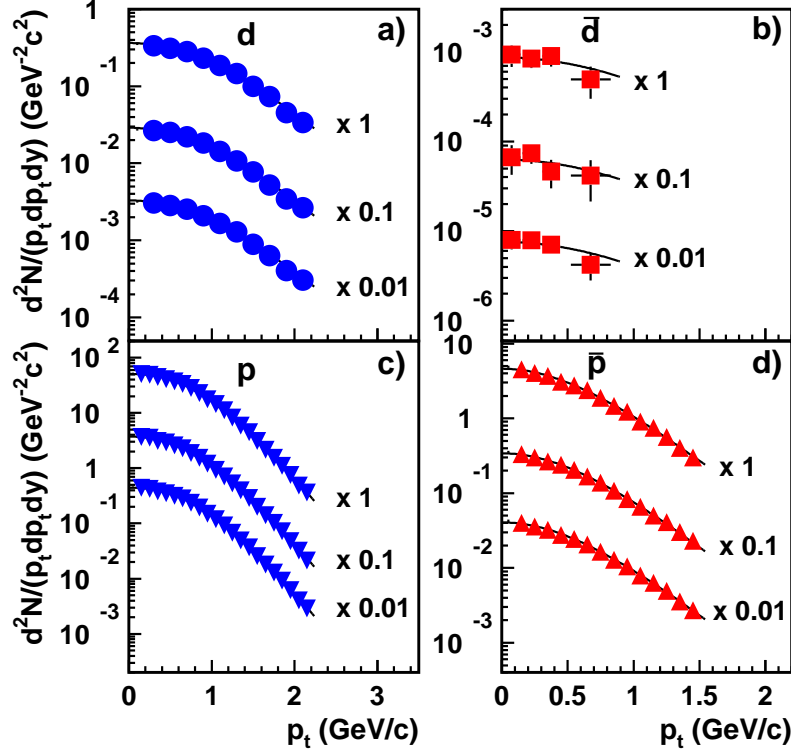


FIG. 4: (Color online) The transverse momentum spectra of deuterons (a), antideuterons (b), protons (c) and antiprotons (d) in centrality selected Pb+Pb collisions at 158A GeV. Only statistical errors are shown. The curves show exponential fits to the data using Eq. (2). Results for the 0-12.5% most central collisions are shown to scale, results for the centrality intervals 12.5 - 23.5 % and 0 - 23.5 % are divided by factors 10 and 10^2 respectively.

the deuteron rest mass.

The small available statistics and resulting limited p_t range for \bar{d} data makes the determination of the slope parameters for \bar{d} less accurate. Thus only the dN/dy parameter was allowed to vary when the \bar{d} spectra were fitted and merely a qualitative comparison of the shape of the spectra is possible. As one can see in Fig. 4 (b), the fits of \bar{d} spectra with slope parameters fixed to the values obtained from the d distributions from the same collision centrality (Fig. 4 (a)) appear to describe the \bar{d} data well. In Fig. 5, the \bar{d}/d ratio for the 0-23% centrality bin is plotted as a function of p_t . The ratio shows little variation with p_t within the errors. A fit with a constant yields an overall \bar{d}/d ratio of $(2.2 \pm 0.2) \cdot 10^{-3}$.

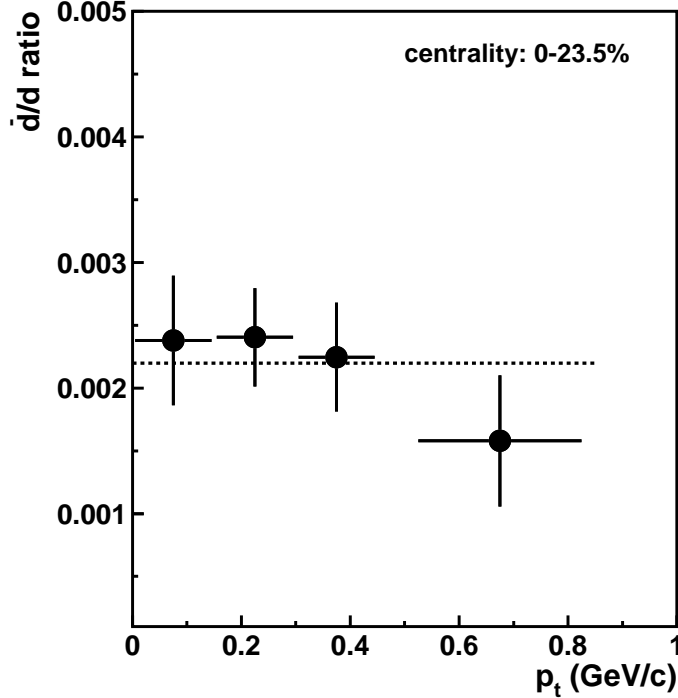


FIG. 5: \bar{d}/d -ratio as a function of p_t in 0-23.5% central Pb+Pb collisions at 158A GeV. The dashed line shows a fit to a constant.

Since no difference in shapes of \bar{d} and d spectra was observed, a likely conclusion is that the dynamical properties of the formation process are the same for d and \bar{d} production. There is also no indication of extra reduction of the \bar{d} yield at low p_t due to annihilation.

The fit parameters dN/dy for the \bar{d} and d spectra in different centrality bins are tabulated in Table II. The fraction of the yield integrated using Eq. 2 over the unmeasured p_t range is $\approx 7\%$ for d and 55% for \bar{d} .

The slope parameter T for deuterons is 406 ± 12 MeV and 391 ± 12 MeV for the 0 - 12.5 % and 12.5 - 23.5 % most central collisions, respectively. It tends to increase with increasing centrality indicating increase of collective transverse flow. In Ref. [13] we reported yields and slopes for deuterons from the 1996 minimum bias data set of Pb+Pb collisions at 158A GeV, subdivided into 6 centrality bins. These measurements for deuterons were obtained in the rapidity range $-0.9 < y < -0.4$, and only tracks with $p_x > 0$ were used. Taking into account the different rapidity intervals for both measurements (an increase of 15% in dN/dy and a decrease of about 5% in T is expected when going from $y = -0.65$ to $y = -0.9$), the overall agreement of the present results with our previously published data is satisfactory.

TABLE II: dN/dy for d and \bar{d} obtained from fits with Eq. (2) in centrality selected Pb+Pb collisions at 158A GeV in the rapidity interval $-1.2 < y < -0.6$. Errors are statistical only.

centrality	deuterons	antideuterons
0 - 12.5 %	0.33 ± 0.02	$(8.1 \pm 1.1) \cdot 10^{-4}$
12.5 - 23.5 %	0.25 ± 0.02	$(5.6 \pm 1.0) \cdot 10^{-4}$
0 - 23.5 %	0.3 ± 0.01	$(6.9 \pm 1.0) \cdot 10^{-4}$

The invariant p_t spectra of $\bar{d}(d)$ are harder than those of $\bar{p}(p)$ [23] (typical $T_p \approx 290 - 300$ MeV). As was pointed out in [19, 22], the characteristic change of the slope with the particle mass is sensitive to the interplay between the density and flow velocity profiles in the source at freeze-out. The observed increase of the inverse slope parameter T of about 30% for d supports a box-like density profile.

B. Rapidity distributions and total yields

Yields of d and \bar{d} as a function of rapidity for the 23.5 % most central Pb+Pb collisions are shown in Fig. 6. There is a difference between the shapes of the rapidity spectra for d and \bar{d} . The observed distinction can be traced back to the longitudinal distributions of their constituents. Data on p and \bar{p} production in centrality selected Pb+Pb collisions at 158A GeV were recently published by NA49 [32]. For collisions of all centralities, the proton rapidity distributions have a dip at midrapidity in contrast to the peak observed for antiprotons. Since the abundance of (anti)clusters (of mass number A) is proportional to the (anti)nucleon phase-space density raised to A^{th} power, the effect of the difference in the shapes of the rapidity distributions is even more pronounced for the composites. In Fig. 6 two Gaussian distributions are plotted for \bar{d} . The dotted line represents the simplest expectation from the coalescence model, namely a Gaussian with a width which is smaller by a factor of $\sqrt{2}$ than that for antiprotons for the centrality class 0-23% [32]. The integral of this distribution is equal to that of the second Gaussian (shown by the dashed line), whose parameters, i.e. the width and total yield were calculated based on the measured points (two unknown parameters and only two measured points). The calculated parameters were found to be $2.4 \cdot 10^{-3}$ for the 4π -yield and 0.95 for the width. The width of the rapidity

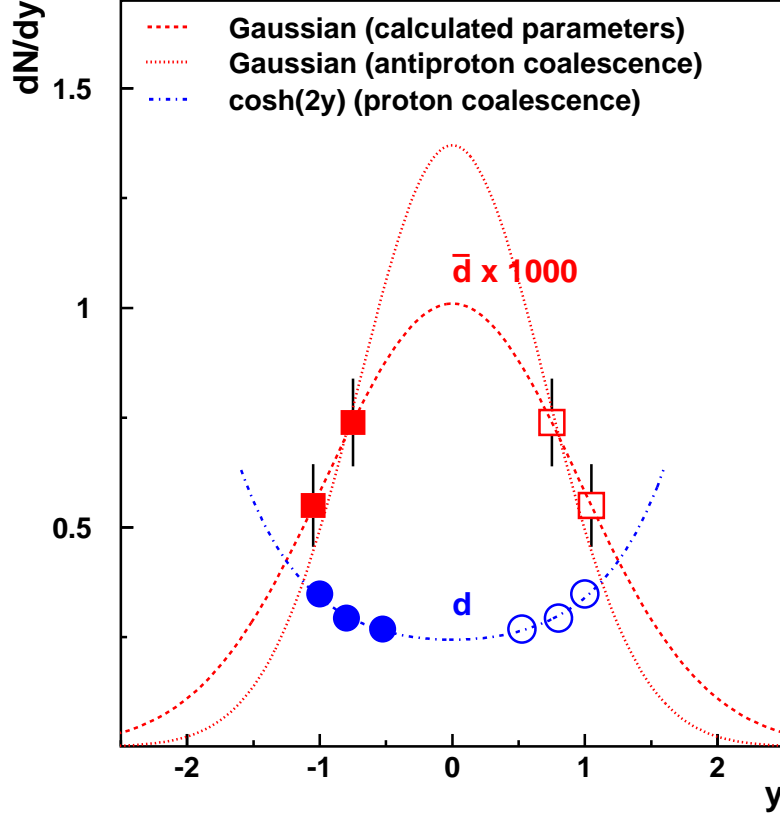


FIG. 6: (Color online) Rapidity distributions for \bar{d} (squares) and d (circles) produced in the 23.5 % most central Pb+Pb collisions at 158A GeV. The solid symbols indicate the measured data points, the open symbols are reflected at midrapidity. The curves represent the results of different fits motivated by a coalescence approach (see text).

distribution for antideuterons is close to that observed for antiprotons ($\sigma_{\bar{p}} \approx 0.93 - 1.03$) in the centrality range under study [32]. For d production the coalescence model predicts a parabolic dependence on rapidity based on that measured for protons [32]. The integral of the parabolic parameterization for d yields 2.8 ± 0.1 .

Rough estimates for the total (anti)cluster yields were made in the framework of a statistical hadron gas model (HGM) [33]. A total yield of 2.5 and $4.6 \cdot 10^{-3}$ was predicted in the 5% most central Pb+Pb collisions at 158A GeV for d and \bar{d} , respectively. Assuming the yield of clusters to scale with the number of wounded nucleons (N_w changes by a factor of about 1.4 from 5% to 23.5% centrality of collisions), the difference between data and the HGM estimates is below 40% for both d and \bar{d} .

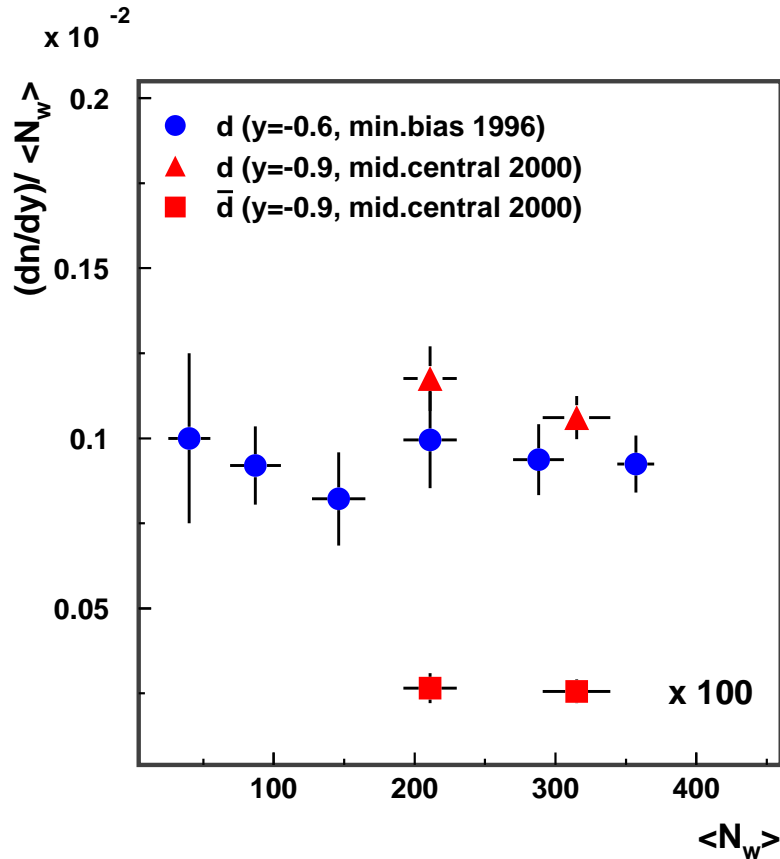


FIG. 7: (Color online) dN/dy divided by the average number of wounded nucleons $\langle N_w \rangle$ for \bar{d} and d for Pb+Pb collisions at 158A GeV.

C. Centrality dependence of \bar{d} and d yields

In Fig. 7 the invariant yield of \bar{d} and d normalized to the number of wounded nucleons $\langle N_w \rangle$ is plotted as a function of $\langle N_w \rangle$. The previously published NA49 results for deuterons from the year 1996 minimum bias data set [13] (blue circles) are also shown. Within the experimental errors, the centrality dependence (if any) of the \bar{d} yield per N_w appears to be weak in mid-central Pb+Pb collisions. Also the normalized yield for d shows little variation in the entire centrality range. This behavior can be understood as an indication of some degree of saturation in the density distribution of both nucleons and antinucleons achieved in mid-central Pb+Pb collisions at the top SPS energy.

D. Coalescence

A combined analysis of the invariant yield spectra of composites and (anti)nucleons has been performed in the framework of a coalescence approach. This approach [16, 17] relates the invariant yield of Z -charged A -clusters (A denotes the atomic mass number and P the momentum) to the product of the yields of protons (p) and neutrons (n) as

$$E_A \frac{d^3 N_A}{d^3 P} = B_A \left(E_p \frac{d^3 N_p}{d^3 p} \right)^Z \left(E_n \frac{d^3 N_n}{d^3 p} \right)^{A-Z} \quad (3)$$

The (unmeasured) yield of neutrons is usually considered to be equal to that of protons; such an assumption seems quite reasonable at SPS energies [31]. Thermal models of cluster production [34, 35] predict the coalescence parameter B_A to be inversely proportional to the volume of the particle source. Such models assume the same freeze-out conditions for matter and antimatter in chemical and thermal equilibrium. More advanced (hydrodynamically motivated) calculations, which implement collective expansion of the reaction zone within the density matrix approach [22] demonstrated a close relation of the characteristic (coalescence) radii to those obtained from 2-particle correlation (HBT) analysis.

Since there is no overlap between the TOF acceptances for (anti)protons and (anti)deuterons (the rapidity coverage of the NA49 TOF detector at 158A GeV is $-1.2 < y < -0.6$ for $d(\bar{d})$ and $-0.5 < y < -0.1$ for $p(\bar{p})$), the (anti)proton spectra measured by TOF were extrapolated to $y = -0.9$. The normalization scaling factors for the p_t spectra were determined using a Gaussian rapidity distribution for antiprotons and a parabolic function for protons. The function parameters were fitted to the experimental data [32]. The shape of the p_t spectra, however, remained unchanged; this assumption is based on the results of [32] which demonstrate that within $|y| < 1$ there is no significant variation in the transverse shape parameters of $p(\bar{p})$ production. In Fig. 8 (numerical values are given in Table III) the coalescence factors B_2 for $d(\bar{d})$ as calculated from Eq. (3) and averaged over the p_t interval 0 - 0.9 GeV/ c are plotted as a function of $\langle N_w \rangle$ for two centrality selected event samples. The B_2 parameters for the $A=2$ nuclei and antinuclei agree within the errors; so the most likely conclusion is that the effective coalescence volumes for clusters and anticlusters are similar. The strong centrality dependence of B_2 might be explained as an increase of the transverse size of the source in more central collisions since in the centrality range under study B_2 approximately scales inversely with N_w .

TABLE III: Coalescence parameters B_2 as calculated from Eq. 3 and averaged over the p_t interval 0 - 0.9 GeV/c for d and \bar{d} in centrality selected Pb+Pb collisions at 158A GeV in the rapidity interval $-1.2 < y < -0.6$. Errors are statistical only.

centrality	0 - 12.5%	12.5 - 23.5%
$\langle N_w \rangle$	315 ± 24	211 ± 19
B_2 (GeV $^2 c^{-3}$) deuterons	$(7.5 \pm 0.4) \cdot 10^{-4}$	$(11.4 \pm 0.5) \cdot 10^{-4}$
B_2 (GeV $^2 c^{-3}$) antideuterons	$(8.3 \pm 1.1) \cdot 10^{-4}$	$(11.6 \pm 2.0) \cdot 10^{-4}$

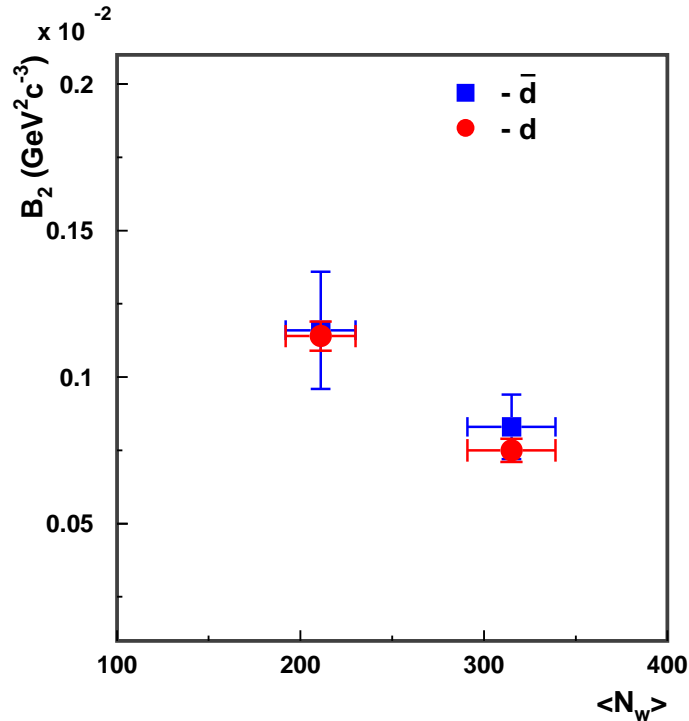


FIG. 8: (Color online) Coalescence parameter B_2 for d and \bar{d} calculated from Eq. 3 in centrality selected Pb+Pb collisions at 158A GeV.

Our measurement of B_2 along with other recent experimental results on the coalescence parameter for antideuterons [36–40] is shown in Fig. 9. Taking into account the variety of experimental conditions for the B_2 measurements (energy, centrality and p_t interval), the experimental data indicate that there is no substantial decrease of the coalescence parameter in the region of $\sqrt{s_{NN}}$ from 17.3 to 200 GeV. This implies that the transverse size of the emitting source for \bar{d} at kinetic freeze-out depends only weakly on $\sqrt{s_{NN}}$ in this energy

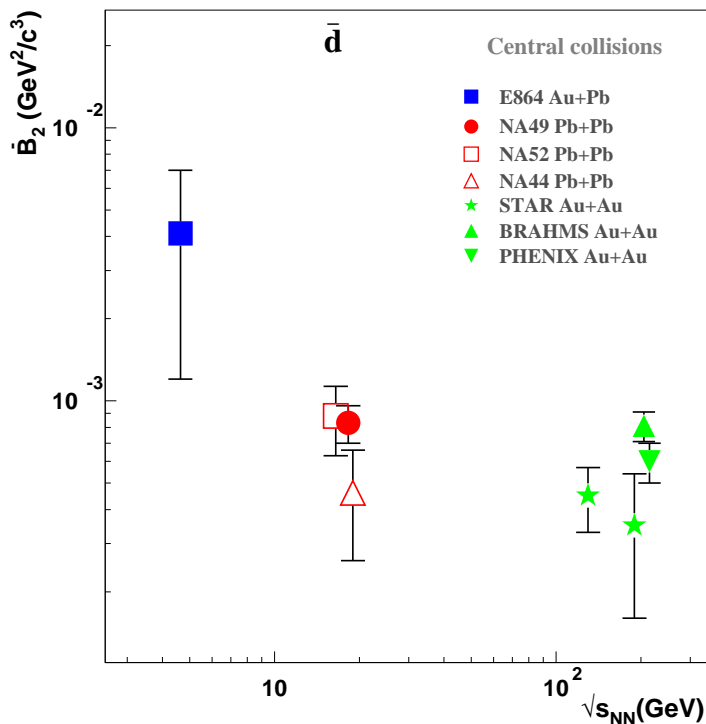


FIG. 9: (Color online) Coalescence parameters B_2 for \bar{d} in central A+A interactions at different collision energies.

domain.

V. SUMMARY

In this paper we present results on \bar{d} and d production in the 23.5 % most central Pb+Pb collisions at 158A GeV. Antideuterons were measured in the rapidity range $-1.2 < y < -0.6$ and transverse momentum interval $0 < p_t < 0.9$ GeV/c. A qualitative comparison of the p_t distributions for \bar{d} and d showed close similarity of spectral shapes at all studied collision centralities. Thus no obvious effects of annihilation in the fireball medium were observed. The rapidity density normalized to the number of wounded nucleons exhibits no centrality dependence for either d or \bar{d} . A difference was observed in the shapes of the rapidity distributions for \bar{d} (convex) and d (concave). The 4π yields were estimated from a Gaussian and parabolic fit for \bar{d} and d , respectively. The extracted coalescence parameters for d and \bar{d} near midrapidity agree with each other within errors, implying a similar freeze-out configuration for matter and antimatter.

Acknowledgments

This work was supported by the US Department of Energy Grant DE-FG03-97ER41020/A000, the Bundesministerium für Bildung und Forschung, Germany (06F 137), the Virtual Institute VI-146 of Helmholtz Gemeinschaft, Germany, the Polish Ministry of Science and Higher Education (1 P03B 006 30, 1 P03B 127 30, 0297/B/H03/2007/33, N N202 078735, N N202 078738, N N202 204638), the Hungarian Scientific Research Foundation (T032648, T032293, T043514), the Hungarian National Science Foundation, OTKA, (F034707), the Bulgarian National Science Fund (Ph-09/05), the Croatian Ministry of Science, Education and Sport (Project 098-0982887-2878) and Stichting FOM, the Netherlands.

References

- [1] U. Heinz *et al.*, J. Phys. G **12** (1986) 1237.
- [2] P. Koch *et al.*, Mod. Phys. Lett. A **3** (1988) 737.
- [3] J. Ellis *et al.*, Phys. Lett. B **233** (1989) 223.
- [4] F. Becattini *et al.*, Phys. Rev. C **73** (2006) 044905.
- [5] M. Bleicher *et al.*, Phys. Lett. B **485** (2000) 133.
- [6] R. Rapp and E. V. Shuryak, Nucl. Phys. A **698** (2002) 587.
- [7] S. Gavin *et al.*, Phys. Lett. B **234** (1990) 175.
- [8] M. J. Bennett *et al.* (E878 Collaboration), Phys. Rev. C **58** (1998) 1155.
- [9] G. Ambrosini *et al.* (NA52 Collaboration), Phys. Lett. B **417** (1998) 202.
- [10] L. Ahle *et al.* (E802 Collaboration), Phys. Rev. C **60** (1999) 064901.
- [11] T. A. Armstrong *et al.* (E864 Collaboration), Phys. Rev. C **61** (2000) 064908.
- [12] J. Barrette *et al.* (E877 Collaboration), Phys. Rev. C **61** (2000) 044906.
- [13] T. Anticic *et al.* (NA49 Collaboration), Phys. Rev. C **69** (2004) 024902.
- [14] T. A. Armstrong *et al.* (E864 Collaboration), Phys. Rev. C **70** (2004) 024902.
- [15] STAR Collaboration, Science **328** (2010) 58.
- [16] S. T. Butler and C. A. Pearson, Phys. Rev. **129** (1963) 836.
- [17] A. Schwarzschild and C. Zupancic, Phys. Rev. **129** (1963) 854.

- [18] C. Alt *et al.* (NA49 Collaboration), Phys. Rev. C **77** (2008) 064908.
- [19] A. Polleri *et al.*, Phys. Lett. B **419** (1998) 19.
- [20] M. Bleicher *et al.*, Phys. Lett. B **361** (1995) 10.
- [21] S. Mrowczynski, Phys. Lett. B **277** (1992) 43.
- [22] R. Scheibl and U. Heinz, Phys. Rev. C **59** (1999) 1585.
- [23] C. Alt *et al.* (NA49 Collaboration), Phys. Rev. C **73** (2006) 044910.
- [24] S. V. Afanasiev *et al.* (NA49 Collaboration), Nucl. Instrum. Meth. A **430** (1999) 210.
- [25] K. Werner, Z. Physik C **42** (1989) 85.
- [26] Details can be found in: <https://edms.cern.ch/file/885329/1/vetocal2.pdf>.
- [27] C. Alt *et al.* (NA49 Collaboration), Phys. Rev. C **78** (2008) 034918.
- [28] T. Anticic *et al.* (NA49 Collaboration), Phys. Rev. C **80** (2009) 034906.
- [29] M. Bleicher *et al.*, J. Phys. G **25** (1999) 1859.
- [30] F. Wang, J. Phys. G **27** (2001) 283.
- [31] V. I. Kolesnikov (for the NA49 Collaboration), J. Phys. Conf. Ser. **110** (2008) 032010.
- [32] T. Anticic *et al.* (NA49 collaboration), Phys. Rev. C **83** (2011) 014901.
- [33] F. Becattini, private communication.
- [34] J. Kapusta, Phys. Rev. C **21** (1980) 1301.
- [35] A. Z. Mekjian, Phys. Rev. C **17** (1978) 1051.
- [36] T. A. Armstrong *et al.* (E864 Collaboration), Phys. Rev. Lett. **85** (2000) 2685.
- [37] I. G. Bearden *et al.* (NA44 Collaboration), Phys. Rev. Lett. **85** (2000) 2681.
- [38] C. Adler *et al.* (STAR Collaboration), Phys. Rev. Lett. **87** (2001) 262301.
- [39] S.S. Adler *et al.* (PHENIX Collaboration), Phys. Rev. Lett. **94** (2005) 122302.
- [40] I. Arsene *et al.* (BRAHMS Collaboration), preprint [nucl-ex] 1005.5427 (2010).

VI. APPENDIX

Tables IV,V,VI and VII list the invariant transverse momentum spectra $d^2N/(p_t dp_t dy)$ in $\text{GeV}^{-2}c^2$ for d , \bar{d} , p and \bar{p} , respectively, in centrality selected Pb+Pb collisions at 158A GeV.

TABLE IV: Transverse momentum spectra $d^2N/(p_t dp_t dy)$ in $\text{GeV}^{-2}c^2$ for deuterons in centrality selected Pb+Pb collisions at 158A GeV averaged over the rapidity interval $-1.2 < y < -0.6$.

p_t	0-12.5%	12.5-23.5%	0-23.5%
0.10	$(3.568 \pm 0.13) \cdot 10^{-1}$	$(2.780 \pm 0.12) \cdot 10^{-1}$	$(3.205 \pm 0.12) \cdot 10^{-1}$
0.30	$(3.360 \pm 0.97) \cdot 10^{-1}$	$(2.667 \pm 0.089) \cdot 10^{-1}$	$(3.041 \pm 0.093) \cdot 10^{-1}$
0.50	$(3.097 \pm 0.12) \cdot 10^{-1}$	$(2.520 \pm 0.11) \cdot 10^{-1}$	$(2.832 \pm 0.11) \cdot 10^{-1}$
0.70	$(2.814 \pm 0.15) \cdot 10^{-1}$	$(2.204 \pm 0.14) \cdot 10^{-1}$	$(2.533 \pm 0.14) \cdot 10^{-1}$
0.90	$(2.301 \pm 0.13) \cdot 10^{-1}$	$(1.830 \pm 0.12) \cdot 10^{-1}$	$(2.084 \pm 0.12) \cdot 10^{-1}$
1.10	$(1.865 \pm 0.11) \cdot 10^{-1}$	$(1.424 \pm 0.095) \cdot 10^{-1}$	$(1.662 \pm 0.10) \cdot 10^{-1}$
1.30	$(1.468 \pm 0.11) \cdot 10^{-1}$	$(1.076 \pm 0.090) \cdot 10^{-1}$	$(1.288 \pm 0.10) \cdot 10^{-1}$
1.50	$(0.991 \pm 0.085) \cdot 10^{-1}$	$(0.776 \pm 0.081) \cdot 10^{-1}$	$(0.892 \pm 0.083) \cdot 10^{-1}$
1.70	$(0.732 \pm 0.076) \cdot 10^{-1}$	$(0.521 \pm 0.066) \cdot 10^{-1}$	$(0.634 \pm 0.072) \cdot 10^{-1}$
1.90	$(0.454 \pm 0.057) \cdot 10^{-1}$	$(0.345 \pm 0.053) \cdot 10^{-1}$	$(0.404 \pm 0.055) \cdot 10^{-1}$
2.10	$(0.339 \pm 0.053) \cdot 10^{-1}$	$(0.264 \pm 0.045) \cdot 10^{-1}$	$(0.306 \pm 0.049) \cdot 10^{-1}$

TABLE V: Transverse momentum spectra $d^2N/(p_t dp_t dy)$ in $\text{GeV}^{-2}c^2$ for antideuterons in centrality selected Pb+Pb collisions at 158A GeV averaged over the rapidity interval $-1.2 < y < -0.6$.

p_t	0-12.5%	12.5-23.5%	0-23.5%
0.075	$(9.33 \pm 2.5) \cdot 10^{-4}$	$(6.67 \pm 2.4) \cdot 10^{-4}$	$(8.00 \pm 1.7) \cdot 10^{-4}$
0.225	$(8.84 \pm 1.8) \cdot 10^{-4}$	$(7.42 \pm 1.8) \cdot 10^{-4}$	$(7.91 \pm 1.3) \cdot 10^{-4}$
0.375	$(9.01 \pm 2.2) \cdot 10^{-4}$	$(4.64 \pm 1.6) \cdot 10^{-4}$	$(7.07 \pm 1.4) \cdot 10^{-4}$
0.675	$(4.92 \pm 1.9) \cdot 10^{-4}$	$(4.17 \pm 2.0) \cdot 10^{-4}$	$(4.21 \pm 1.4) \cdot 10^{-4}$

TABLE VI: Transverse momentum spectra $d^2N/(p_t dp_t dy)$ in $\text{GeV}^{-2}c^2$ for protons in centrality selected Pb+Pb collisions at 158A GeV averaged over the rapidity interval $-0.5 < y < -0.1$.

p_t	0-12.5%	12.5-23.5%	0-23.5%
0.05	(52.84 ± 0.90)	(38.64 ± 0.54)	(46.01 ± 0.73)
0.15	(50.74 ± 0.52)	(36.82 ± 0.31)	(44.04 ± 0.42)
0.25	(48.85 ± 0.48)	(35.44 ± 0.29)	(42.39 ± 0.39)
0.35	(44.41 ± 0.49)	(31.19 ± 0.29)	(38.05 ± 0.39)
0.45	(40.86 ± 0.49)	(29.28 ± 0.29)	(35.28 ± 0.39)
0.55	(37.11 ± 0.44)	(26.06 ± 0.26)	(31.79 ± 0.36)
0.65	(33.69 ± 0.40)	(23.01 ± 0.23)	(28.55 ± 0.32)
0.75	(28.19 ± 0.35)	(18.69 ± 0.20)	(23.62 ± 0.28)
0.85	(22.94 ± 0.30)	(15.42 ± 0.18)	(19.32 ± 0.24)
0.95	(17.72 ± 0.26)	(12.09 ± 0.15)	(15.01 ± 0.21)
1.05	(14.43 ± 0.22)	(9.288 ± 0.15)	(11.95 ± 0.18)
1.15	(11.12 ± 0.19)	(7.138 ± 0.11)	(9.205 ± 0.15)
1.25	(8.181 ± 0.16)	(5.312 ± 0.089)	(6.799 ± 0.12)
1.35	(5.874 ± 0.13)	(3.950 ± 0.074)	(4.947 ± 0.10)
1.45	(4.459 ± 0.11)	(2.899 ± 0.061)	(3.708 ± 0.086)
1.55	(3.083 ± 0.089)	(1.901 ± 0.050)	(2.557 ± 0.071)
1.65	(2.162 ± 0.079)	(1.415 ± 0.045)	(1.802 ± 0.063)
1.75	(1.535 ± 0.070)	(1.028 ± 0.040)	(1.291 ± 0.056)
1.85	(1.096 ± 0.064)	(0.723 ± 0.036)	(0.916 ± 0.050)
1.95	(0.749 ± 0.058)	(0.477 ± 0.032)	(0.618 ± 0.046)
2.05	(0.486 ± 0.051)	(0.320 ± 0.029)	(0.406 ± 0.040)

TABLE VII: Transverse momentum spectra $d^2N/(p_t dp_t dy)$ in $\text{GeV}^{-2}c^2$ for antiprotons in centrality selected Pb+Pb collisions at 158A GeV averaged over the rapidity interval $-0.5 < y < -0.1$.

p_t	0-12.5%	12.5-23.5%	0-23.5%
0.05	(4.819 ± 0.24)	(3.507 ± 0.15)	(4.221 ± 0.20)
0.15	(4.548 ± 0.14)	(3.323 ± 0.086)	(3.991 ± 0.11)
0.25	(4.044 ± 0.12)	(3.003 ± 0.074)	(3.574 ± 0.097)
0.35	(3.694 ± 0.12)	(2.654 ± 0.074)	(3.223 ± 0.100)
0.45	(3.076 ± 0.11)	(2.395 ± 0.071)	(2.774 ± 0.094)
0.55	(2.743 ± 0.11)	(2.054 ± 0.066)	(2.434 ± 0.088)
0.65	(2.377 ± 0.099)	(1.679 ± 0.059)	(2.060 ± 0.079)
0.75	(1.871 ± 0.085)	(1.377 ± 0.052)	(1.649 ± 0.069)
0.85	(1.470 ± 0.074)	(1.073 ± 0.045)	(1.291 ± 0.060)
0.95	(1.226 ± 0.065)	(0.833 ± 0.038)	(1.046 ± 0.052)
1.05	(0.907 ± 0.056)	(0.659 ± 0.033)	(0.794 ± 0.045)
1.15	(0.743 ± 0.050)	(0.500 ± 0.029)	(0.632 ± 0.040)
1.25	(0.562 ± 0.045)	(0.411 ± 0.027)	(0.494 ± 0.037)
1.35	(0.401 ± 0.041)	(0.304 ± 0.025)	(0.358 ± 0.033)
1.45	(0.302 ± 0.038)	(0.231 ± 0.024)	(0.271 ± 0.031)